

# A new methodology for the discrete analysis of concrete fracture under impact loading

G.N.Wells & L.J.Sluys

Koiter Institute Delft, Delft University of Technology, The Netherlands

**ABSTRACT:** A newly developed numerical model for simulating arbitrary displacement discontinuities is extended for the case of dynamic loading. The model involves the addition of the Heaviside jump to the underlying finite element interpolation basis functions. A displacement jump is continuous across element boundaries and the order of the displacement jump interpolation is the same as the underlying element. The finite element formulation for dynamic problems is developed in a consistent manner from the weak equation of motion, which leads naturally to stiffness and mass matrices which involve discontinuous terms. The model is used to simulate the propagation of cohesive cracks in concrete under impact loading. Analyses are shown to be independent of the spatial discretisation and the performance is excellent with very coarse finite element meshes. The numerical simulations of a double-notched specimen compare well with experimental results.

## 1 INTRODUCTION

The cohesive zone concept has proved popular for simulating failure in concrete. Inelastic deformations in the continuum are compressed onto a line, across which the displacement field is assumed to be discontinuous. The tractions acting at the surface are then made functions of the displacement jump. This type of model was first proposed by Dugdale (1960) and Barenblatt (1962) for representing fracture in elastoplastic solids. The cohesive zone concept has several attractive features for the analysis of concrete. By having tractions acting at a discontinuity, the stress singularity that arises when considering sharp cracks in an elastic body is avoided. This allows accurate calculations with relatively coarse finite element meshes since very high strain gradients are avoided. Further, the cohesive zone concept allows inelastic behaviour to be modelled in a simple manner.

The cohesive zone (or fictitious crack) concept was used by Hillerborg, Modér, and Petersson (1976) for the analysis of failure in concrete. An attractive feature of such a formulation is its simplicity, with the constitutive response at an interface governed by two key material parameters: the tensile strength and the fracture energy. The most significant difficulty in using the cohesive zone concept for fracture simulations is modelling a displacement discontinuity whose path is not known a priori. Traditionally, a discontinuity has been modelled using either interface elements (Schellekens and De Borst 1993) or through explicit modifications of the mesh to capture the discontinuity

(Swenson and Ingraffea 1988). In this work, the model recently developed in Wells and Sluys (2001b) for simulating displacement discontinuities that cross through solid finite elements is extended to the case of dynamic loading.

A discontinuous displacement field can be described mathematically using discontinuous functions, with the displacement field decomposed into continuous and discontinuous parts. Inserting the decomposed displacement field into the weak governing equations leads in a natural fashion to two separate variational equations. The discretised discontinuous displacement field falls within the partition of unity concept (Babuška and Melenk 1997; Duarte and Oden 1996). The method was used by Wells and Sluys (2001b) to simulate cohesive cracks under quasi-static loading. Numerical examples test the method for objectivity with respect to finite element mesh alignment and element size under impact loading, and comparisons are made with experimental results.

## 2 KINEMATIC DESCRIPTION

The displacement field for a body crossed by a single discontinuity (see figure 1) can be described by:

$$\mathbf{u}(\mathbf{x}, t) = \hat{\mathbf{u}}(\mathbf{x}, t) + \mathcal{H}_{\Gamma_d}(\mathbf{x})\bar{\mathbf{u}}(\mathbf{x}, t) \quad (1)$$

where  $\hat{\mathbf{u}}$  and  $\bar{\mathbf{u}}$  are continuous functions on  $\Omega$  and  $\mathcal{H}_{\Gamma_d}$  is the Heaviside jump centred at the discontinuity surface  $\Gamma_d$  ( $\mathcal{H}_{\Gamma_d} = 1 \ \mathbf{x} \in \Omega^+$ ,  $\mathcal{H}_{\Gamma_d} = 0 \ \mathbf{x} \in \Omega^-$ ).

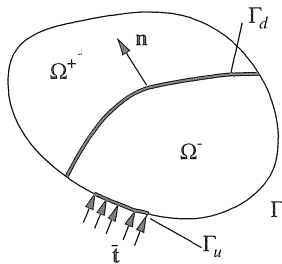


Figure 1: Body  $\Omega$  crossed by a displacement discontinuity  $\Gamma_d$ .

The corresponding acceleration field is found by differentiating equation (1) twice with respect to time. Assuming that the Heaviside function is stationary ( $d\mathcal{H}_{\Gamma_d}/dt = 0$ ), the acceleration field is given by:

$$\ddot{\mathbf{u}}(\mathbf{x}, t) = \ddot{\mathbf{u}}(\mathbf{x}, t) + \mathcal{H}_{\Gamma_d}(\mathbf{x})\ddot{\mathbf{u}}(\mathbf{x}, t). \quad (2)$$

The infinitesimal strain field can be found by taking the symmetric gradient of the displacement field in equation (1), again assuming that the Heaviside function is stationary. This leads to:

$$\boldsymbol{\varepsilon} = \nabla^s \hat{\mathbf{u}} + \mathcal{H}_{\Gamma_d} \nabla^s \tilde{\mathbf{u}} + \delta_{\Gamma_d} (\tilde{\mathbf{u}} \otimes \mathbf{n})^s \quad (3)$$

where  $\delta_{\Gamma_d}$  is the Dirac-delta distribution, centred at the discontinuity  $\Gamma_d$  and  $\mathbf{n}$  is the normal vector to the discontinuity, pointing to  $\Omega^+$ .

It was shown by Bažant and Belytschko (1985) that the Dirac-delta distribution arises in the strain field of the analytical solution for a wave travelling in a strain softening bar. Based on the preceding kinematic description, the presence of the Dirac-delta distribution implies the development of a displacement discontinuity. The presence of the Dirac-delta distribution should therefore not be interpreted as a spurious response, rather it indicates the necessity of a change from a continuum stress-strain relationship to a discrete traction-separation relationship at a surface.

For finite element implementation, the displacement and acceleration fields must be expressed in a discretised format. In terms of nodal values, the displacement field in equation (1) and the acceleration field in equation (2) are expressed as:

$$\mathbf{u} = \mathbf{N}\mathbf{a} + \mathcal{H}_{\Gamma_d} \mathbf{N}\mathbf{b} \quad (4a)$$

$$\ddot{\mathbf{u}} = \mathbf{N}\ddot{\mathbf{a}} + \mathcal{H}_{\Gamma_d} \mathbf{N}\ddot{\mathbf{b}} \quad (4b)$$

where  $\mathbf{N}$  is a matrix containing the usual element shape functions,  $\mathbf{a}$  are the regular nodal degrees of

freedom and  $\mathbf{b}$  are ‘enhanced’ nodal degrees of freedom. The discretisation involves two sets of degrees of freedom at a node: regular and enhanced. The function  $\hat{\mathbf{u}}$  is interpolated by  $\mathbf{N}\mathbf{a}$  and the function  $\tilde{\mathbf{u}}$  by  $\mathbf{N}\mathbf{b}$ . The displacement jump at a discontinuity is given by  $\mathbf{N}\mathbf{b}$ ,  $\mathbf{x} \in \Gamma_d$ . Formally, the interpolation in equation (4b) can be interpreted as an interpolation based on the partition of unity concept (Babuška and Melnik 1997; Duarte and Oden 1996; Wells and Sluys 2001b).

To express the strain field in a discretised format, it is necessary to express the functions  $\nabla^s \hat{\mathbf{u}}$  and  $\nabla^s \tilde{\mathbf{u}}$  in terms of nodal degrees of freedom,

$$\nabla^s \hat{\mathbf{u}} = \mathbf{B}\mathbf{a} \quad (5a)$$

$$\nabla^s \tilde{\mathbf{u}} = \mathbf{B}\mathbf{b} \quad (5b)$$

where  $\mathbf{B}$  is the usual matrix containing spatial derivatives of the element shape functions.

### 3 FINITE ELEMENT FORMULATION

To develop a finite element model, the kinematic decompositions from the previous section must be inserted into the weak equation of motion. This provides a firm theoretical basis for the model. The weak form of the equation of motion, without body forces, is written as:

$$\int_{\Omega} \nabla^s \boldsymbol{\eta} : \boldsymbol{\sigma} \, d\Omega + \int_{\Omega} \boldsymbol{\eta} \cdot \rho \ddot{\mathbf{u}} \, d\Omega = \int_{\Gamma_u} \boldsymbol{\eta} \cdot \bar{\mathbf{t}} \, d\Gamma \quad (6)$$

where  $\boldsymbol{\eta}$  are admissible displacement variations,  $\boldsymbol{\sigma}$  is the stress field,  $\bar{\mathbf{t}}$  are external traction forces, applied on the boundary  $\Gamma_u$  (see figure 1) and  $\rho$  is the density. Taking the space of admissible displacement variations the same as actual displacements (a Galerkin formulation), from equation (1), variations of displacement,  $\boldsymbol{\eta}$ , are decomposed as:

$$\boldsymbol{\eta} = \hat{\boldsymbol{\eta}} + \mathcal{H}_{\Gamma_d} \tilde{\boldsymbol{\eta}}. \quad (7)$$

From equation (3), the gradient of admissible displacement variations is expressed as:

$$\nabla^s \boldsymbol{\eta} = \nabla^s \hat{\boldsymbol{\eta}} + \mathcal{H}_{\Gamma_d} \nabla^s \tilde{\boldsymbol{\eta}} + \delta_{\Gamma_d} (\tilde{\boldsymbol{\eta}} \otimes \mathbf{n})^s. \quad (8)$$

Inserting equations (7) and (8) and the acceleration field from equation (2) into the weak equation of motion (6) leads to:

$$\begin{aligned} & \int_{\Omega} \nabla^s (\hat{\boldsymbol{\eta}} + \mathcal{H}_{\Gamma_d} \tilde{\boldsymbol{\eta}}) : \boldsymbol{\sigma} \, d\Omega \\ & + \int_{\Omega} (\hat{\boldsymbol{\eta}} + \mathcal{H}_{\Gamma_d} \tilde{\boldsymbol{\eta}}) \cdot \rho (\ddot{\mathbf{u}} + \mathcal{H}_{\Gamma_d} \ddot{\tilde{\mathbf{u}}}) \, d\Omega \\ & = \int_{\Gamma_u} (\hat{\boldsymbol{\eta}} + \mathcal{H}_{\Gamma_d} \tilde{\boldsymbol{\eta}}) \cdot \bar{\mathbf{t}} \, d\Gamma. \quad (9) \end{aligned}$$

Requiring that equation (6) holds for any admissible variation  $\boldsymbol{\eta}$  implies that equation (9) must hold for any admissible variations  $\hat{\boldsymbol{\eta}}$  and  $\tilde{\boldsymbol{\eta}}$ . Taking the gradient of variations of displacements (see equation (8)), and rearranging, equation (9) can be expressed as:

$$\begin{aligned} & \int_{\Omega} \nabla^s \hat{\boldsymbol{\eta}} : \boldsymbol{\sigma} \, d\Omega + \int_{\Omega} \mathcal{H}_{\Gamma_d} (\nabla^s \tilde{\boldsymbol{\eta}}) : \boldsymbol{\sigma} \, d\Omega \\ & + \int_{\Omega} \delta_{\Gamma_d} (\hat{\boldsymbol{\eta}} \otimes \mathbf{n})^s : \boldsymbol{\sigma} \, d\Omega + \int_{\Omega} \hat{\boldsymbol{\eta}} \cdot \rho \ddot{\mathbf{u}} \, d\Omega \\ & + \int_{\Omega} \mathcal{H}_{\Gamma_d} \hat{\boldsymbol{\eta}} \cdot \rho \ddot{\mathbf{u}} \, d\Omega + \int_{\Omega} \mathcal{H}_{\Gamma_d} \tilde{\boldsymbol{\eta}} \cdot \rho \ddot{\mathbf{u}} \, d\Omega \\ & + \int_{\Omega} \mathcal{H}_{\Gamma_d} \tilde{\boldsymbol{\eta}} \cdot \rho \ddot{\mathbf{u}} \, d\Omega = \int_{\Gamma_u} (\hat{\boldsymbol{\eta}} + \mathcal{H}_{\Gamma_d} \tilde{\boldsymbol{\eta}}) \cdot \bar{\mathbf{t}} \, d\Gamma. \quad (10) \end{aligned}$$

Changing the integral whose integrand contains the Dirac-delta term from a volume integral to a surface integral to eliminate the Dirac-delta term (using integral properties of the Dirac-delta distribution) and eliminating the Heaviside function by changing the integration domain of integrals whose integrand contains the Heaviside function from  $\Omega$  to  $\Omega^+$  (see figure 1),

$$\begin{aligned} & \int_{\Omega} \nabla^s \hat{\boldsymbol{\eta}} : \boldsymbol{\sigma} \, d\Omega + \int_{\Omega^+} \nabla^s \tilde{\boldsymbol{\eta}} : \boldsymbol{\sigma} \, d\Omega \\ & + \int_{\Gamma_d} \tilde{\boldsymbol{\eta}}_{\Gamma_d} \cdot \mathbf{t} \, d\Gamma + \int_{\Omega} \hat{\boldsymbol{\eta}} \cdot \rho \ddot{\mathbf{u}} \, d\Omega + \int_{\Omega^+} \hat{\boldsymbol{\eta}} \cdot \rho \ddot{\mathbf{u}} \, d\Omega \\ & + \int_{\Omega^+} \tilde{\boldsymbol{\eta}} \cdot \rho \ddot{\mathbf{u}} \, d\Omega + \int_{\Omega^+} \tilde{\boldsymbol{\eta}} \cdot \rho \ddot{\mathbf{u}} \, d\Omega \\ & = \int_{\Gamma_u} (\hat{\boldsymbol{\eta}} + \mathcal{H}_{\Gamma_d} \tilde{\boldsymbol{\eta}}) \cdot \bar{\mathbf{t}} \, d\Gamma \quad (11) \end{aligned}$$

where  $\mathbf{t}$  ( $= \boldsymbol{\sigma} \mathbf{n}$ ) are the traction forces acting at the surface  $\Gamma_d$ . Taking first variations  $\hat{\boldsymbol{\eta}}$  ( $\tilde{\boldsymbol{\eta}} = \mathbf{0}$ ) and then variations  $\tilde{\boldsymbol{\eta}}$  ( $\hat{\boldsymbol{\eta}} = \mathbf{0}$ ), two separate variational statements can be formed:

$$\begin{aligned} & \int_{\Omega} \nabla^s \hat{\boldsymbol{\eta}} : \boldsymbol{\sigma} \, d\Omega + \int_{\Omega} \hat{\boldsymbol{\eta}} \cdot \rho \ddot{\mathbf{u}} \, d\Omega + \int_{\Omega^+} \hat{\boldsymbol{\eta}} \cdot \rho \ddot{\mathbf{u}} \, d\Omega \\ & = \int_{\Gamma_u} \hat{\boldsymbol{\eta}} \cdot \bar{\mathbf{t}} \, d\Gamma \quad (12a) \end{aligned}$$

$$\begin{aligned} & \int_{\Omega^+} \nabla^s \tilde{\boldsymbol{\eta}} : \boldsymbol{\sigma} \, d\Omega + \int_{\Gamma_d} \tilde{\boldsymbol{\eta}}_{\Gamma_d} \cdot \mathbf{t} \, d\Gamma + \int_{\Omega^+} \tilde{\boldsymbol{\eta}} \cdot \rho \ddot{\mathbf{u}} \, d\Omega \\ & + \int_{\Omega^+} \tilde{\boldsymbol{\eta}} \cdot \rho \ddot{\mathbf{u}} \, d\Omega = \int_{\Gamma_u} \mathcal{H}_{\Gamma_d} \tilde{\boldsymbol{\eta}} \cdot \bar{\mathbf{t}} \, d\Gamma. \quad (12b) \end{aligned}$$

The equations in (12) represent a coupled problem, with the two equations coupled through their dependence on the stress field. Considering a small volume crossed by a discontinuity, equation (12b) ensures that the weak equation of motion is satisfied in a weak sense across a discontinuity (Wells and Sluys 2001a).

Inserting the discretised expressions for the functions  $\hat{\mathbf{u}}$  and  $\tilde{\mathbf{u}}$  and their gradients from equations (4b) and (5) into equation (12) leads to two discrete weak governing equations:

$$\begin{aligned} & \int_{\Omega} \mathbf{B}^T \boldsymbol{\sigma} \, d\Omega + \int_{\Omega} \mathbf{N}^T \rho \mathbf{N} \ddot{\mathbf{a}} \, d\Omega + \int_{\Omega^+} \mathbf{N}^T \rho \mathbf{N} \ddot{\mathbf{b}} \, d\Omega \\ & = \int_{\Gamma_u} \mathbf{N}^T \bar{\mathbf{t}} \, d\Gamma \quad (13a) \end{aligned}$$

$$\begin{aligned} & \int_{\Omega^+} \mathbf{B}^T \boldsymbol{\sigma} \, d\Omega + \int_{\Gamma_d} \mathbf{N}^T \mathbf{t} \, d\Gamma + \int_{\Omega^+} \mathbf{N}^T \rho \mathbf{N} \ddot{\mathbf{a}} \, d\Omega \\ & + \int_{\Omega^+} \mathbf{N}^T \rho \mathbf{N} \ddot{\mathbf{b}} \, d\Omega = \int_{\Gamma_u} \mathcal{H}_{\Gamma_d} \mathbf{N}^T \bar{\mathbf{t}} \, d\Gamma. \quad (13b) \end{aligned}$$

The stress rate in the continuum in terms of nodal velocities is expressed as:

$$\dot{\boldsymbol{\sigma}} = \mathbf{D} (\mathbf{B} \dot{\mathbf{a}} + \mathcal{H}_{\Gamma_d} \mathbf{B} \dot{\mathbf{b}}) \quad (14)$$

where  $\mathbf{D}$  is the material tangent which relates the instantaneous stress and strain rates. The traction rate at a discontinuity is expressed as:

$$\dot{\mathbf{t}} = \mathbf{T} \mathbf{N} \dot{\mathbf{b}} \quad (15)$$

where  $\mathbf{T}$  relates the instantaneous traction and displacement jump rates. Inserting the stress and traction rate expression into the discretised weak governing equations leads to:

$$\mathbf{M} \begin{Bmatrix} \dot{\mathbf{a}}^{t+dt} \\ \dot{\mathbf{b}}^{t+dt} \end{Bmatrix} + \mathbf{K} \begin{Bmatrix} d\mathbf{a} \\ d\mathbf{b} \end{Bmatrix} = \begin{Bmatrix} \mathbf{f}_{\text{ext},a}^{t+dt} \\ \mathbf{f}_{\text{ext},b}^{t+dt} \end{Bmatrix} - \begin{Bmatrix} \mathbf{f}_{\text{int},a}^t \\ \mathbf{f}_{\text{int},b}^t \end{Bmatrix} \quad (16)$$

where the stiffness matrix  $\mathbf{K}$  has the form:

$$\mathbf{K} = \begin{bmatrix} \int_{\Omega} \mathbf{B}^T \mathbf{D} \mathbf{B} \, d\Omega & \int_{\Omega^+} \mathbf{B}^T \mathbf{D} \mathbf{B} \, d\Omega \\ \int_{\Omega^+} \mathbf{B}^T \mathbf{D} \mathbf{B} \, d\Omega & \int_{\Omega^+} \mathbf{B}^T \mathbf{D} \mathbf{B} \, d\Omega + \int_{\Gamma_d} \mathbf{N}^T \mathbf{T} \mathbf{N} \, d\Gamma \end{bmatrix} \quad (17)$$

the consistent mass matrix  $\mathbf{M}$  has the form:

$$\mathbf{M} = \begin{bmatrix} \int_{\Omega} \rho \mathbf{N}^T \mathbf{N} d\Omega & \int_{\Omega^+} \rho \mathbf{N}^T \mathbf{N} d\Omega \\ \int_{\Omega^+} \rho \mathbf{N}^T \mathbf{N} d\Omega & \int_{\Omega^+} \rho \mathbf{N}^T \mathbf{N} d\Omega \end{bmatrix} \quad (18)$$

and the internal and external force vectors are equal to:

$$\mathbf{f}_{\text{ext},a} = \int_{\Gamma_u} \mathbf{N}^T \bar{\mathbf{t}} d\Gamma \quad (19a)$$

$$\mathbf{f}_{\text{ext},b} = \int_{\Gamma_u} \mathcal{H}_{\Gamma_d} \mathbf{N}^T \bar{\mathbf{t}} d\Gamma \quad (19b)$$

$$\mathbf{f}_{\text{int},a} = \int_{\Omega} \mathbf{B}^T \boldsymbol{\sigma} d\Omega \quad (19c)$$

$$\mathbf{f}_{\text{int},b} = \int_{\Omega^+} \mathbf{B}^T \boldsymbol{\sigma} d\Omega + \int_{\Gamma_d} \mathbf{N}^T \bar{\mathbf{t}} d\Gamma. \quad (19d)$$

Note the effect of the Heaviside jump on the semi-discrete system of equations in equation (16). Both the stiffness matrix and the mass matrix contain integrals over the domain  $\Omega^+$ , reflecting the presence of the Heaviside jump in the formulation. The influence of a displacement jump is ‘felt’ in both the mechanical forces due to stresses and in the inertial forces.

#### 4 IMPLEMENTATION ASPECTS

The key to numerical implementation is the addition of extra degrees of freedom to existing element nodes to represent a discontinuity. Since away from a discontinuity, the Heaviside jump resembles a constant function, activating the  $\mathbf{b}$  degrees of freedom at all nodes would lead to a stiffness matrix which is not positive definite, as a constant function is included in the basis of the element shape functions. Therefore, the extra degrees of freedom are activated only at nodes whose support is crossed by a discontinuity. This is illustrated in figure 2. For the same reason, the integration scheme in elements may need to be adjusted to ensure both sides of the discontinuity are adequately integrated. Details of the integration scheme can be found in Wells and Sluys (2001b). As a discontinuity propagates through a mesh, enhanced degrees of freedom are activated. It is stressed that no additional nodes are created, simply degrees of freedom are activated at existing nodes. Since extra degrees are added only to nodes near a discontinuity, the method is potentially very efficient since relatively few extra degrees of freedom are added.

An important requirement is that the displacement jump be equal to zero at a discontinuity tip. This can be enforced by requiring that discontinuity tips coincide with element boundaries and not activating the enhanced degrees of freedom on the element edge ‘touched’ by the discontinuity (see figure 2). It is possible to simulate discontinuities whose tips lie in-

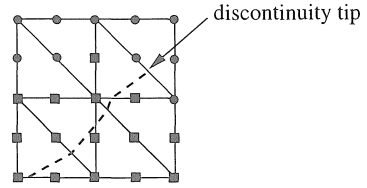


Figure 2: Patch of quadratic triangular elements crossed by a discontinuity (dashed line). The square nodes have extra degrees of freedom to represent the discontinuity.

side elements, although this is not advisable when using incremental solution procedures (Wells and Sluys 2001b). A further restriction is applied which simplifies the numerical implementation. Where essential boundary conditions are applied,  $\bar{\mathbf{u}} = \mathbf{0}$ . This allows essential boundary conditions to be applied in the same fashion as for conventional finite elements.

It is stressed that the proposed method results in a displacement jump whose magnitude is continuous across element boundaries. To this point, no assumptions have been made regarding the underlying solid element type. The order of the displacement jump interpolation along a discontinuity is equal to the polynomial order of the underlying base element.

#### 5 COHESIVE INTERFACE MODEL

A discontinuity is assumed to extend when the maximum principal stress at any integration point in the element ahead of a discontinuity tip exceeds the tensile strength of the material,  $f_t$ . A discontinuity extension is aligned perpendicular to the maximum principal stress direction.

The traction–separation response at an interface is similar to that used by Hillerborg, Modeer, and Petersson (1976), and is a simplified version of that used by Wells and Sluys (2001c). The model presented here is for the two-dimensional case. For loading, the traction transmitted normal to a discontinuity,  $t_n$ , is given by:

$$t_n = f_t \exp\left(-\frac{f_t}{G_f} \kappa\right) \quad (20)$$

where  $\kappa$  is the largest value of the normal opening displacement ( $\bar{u}_n$ ,  $\mathbf{x} \in \Gamma_d$ ) reached and  $G_f$  is the fracture energy. The shear (sliding) traction at an interface  $t_s$  is given by:

$$t_s = k_s \bar{u}_s \quad \mathbf{x} \in \Gamma_d \quad (21)$$

where  $k_s$  is a constant stiffness. Unlike the model used in Wells and Sluys (2001c), the sliding stiffness here is not a function of the opening displacement. This preserves symmetry of the global stiffness matrix for the proposed model. For unloading, the secant stiffness is used.

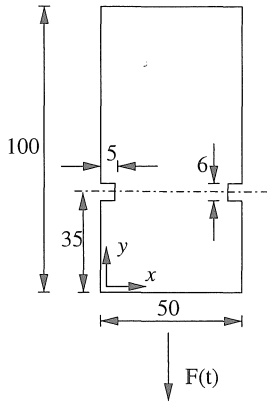


Figure 3: Double-notched specimen analysed under impact loading.

### 6 NUMERICAL EXAMPLES

To illustrate the model, a concrete double-notched tensile specimen, subjected to a tensile impact load, is analysed. The specimen is analysed using different finite element meshes to test objectivity with respect to spatial discretisation. The six-noded triangle is used as the underlying base element and plane strain conditions are assumed. Time integration is performed using the Newmark scheme ( $\beta = 0.25, \gamma = 0.5$ ) and a full Newton-Raphson procedure is used.

The specimen, which is shown in figure 3, was tested experimentally by Weerheijm (1992). The experimental tests were performed using a split-Hopkinson bar apparatus. The split-Hopkinson bar is approximately 10 metres in length, while the concrete specimen is 100 mm in height. The split-Hopkinson bar is very long in order to avoid reflection of the stress wave travelling in the bar at the fixed boundaries during failure of the concrete specimen. To avoid simulating the entire bar, the bar is modelled as shown in figure 4. This arrangement was used by Sluys and De Borst (1996). Further from the bar, the Young's modulus is reduced and the density increased in order to slow the stress wave travelling in the bar. The properties of the bar are chosen such that the acoustic impedance is constant, avoiding reflections at the boundary between the parts of the bar with different material parameters.

The material parameters for the concrete, taken from Sluys and De Borst (1996), are: Young's modulus  $E = 40.7 \times 10^3$  MPa, Poisson's ratio  $\nu = 0.2$ , tensile strength  $f_t = 4.9$  MPa, density  $\rho = 2.35 \times 10^{-9}$  Ns/mm<sup>4</sup> and fracture energy  $G_f = 0.25$  N/m. A low shear sliding stiffness of  $k_s = 1 \times 10^{-4}$  N/mm<sup>3</sup> is adopted. The Young's modulus, tensile strength and fracture energy are all higher than usual for concrete under static loading. The parameters are based on empirical adjustments to account for the higher strength

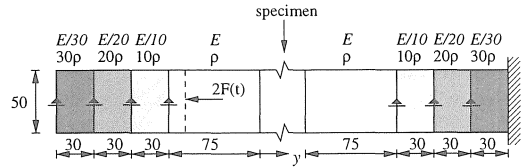


Figure 4: Model representation of the split-Hopkinson bar.

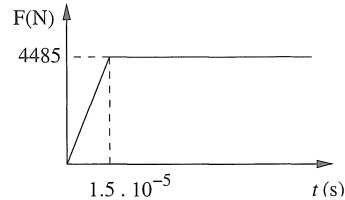


Figure 5: Loading as a function of time for the double-notched analysis.

and stiffness of concrete under impact loading. A time step of  $\Delta t = 1.0 \times 10^{-6}$  s is used. The applied load, as a function of time, is shown in figure 5. Two different finite element meshes are used for the analysis. The first is composed of 214 elements, and the second of 958 elements. The two meshes are shown in figure 6. Recall that with quadratic base elements, the interpolation order for the displacement jump is quadratic.

Two particular failure cases are analysed. The first is symmetric failure, in which discontinuities propagate from both notches and meet in the centre of the specimen. The results of this analysis using the two different meshes, compared to experimentally measured results from Weerheijm (1992), are shown in figure 7. It is clear that the results for the two meshes are near identical and compare very well to the experimental results. The second failure case is non-symmetric, with a single crack propagating from one notch only. The results for the case of non-

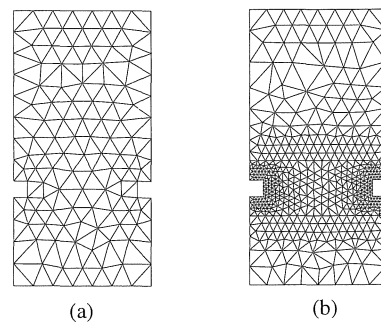


Figure 6: Finite element meshes used for the double-notched specimen with (a) 214 elements and (b) 958 elements. The element interpolation order is quadratic.

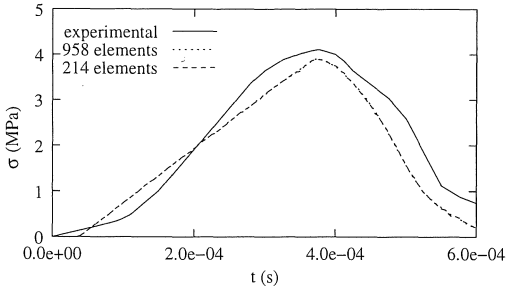


Figure 7: Calculated normal stress transmitted across at the top boundary of the specimen for the symmetric failure case and experimental results.

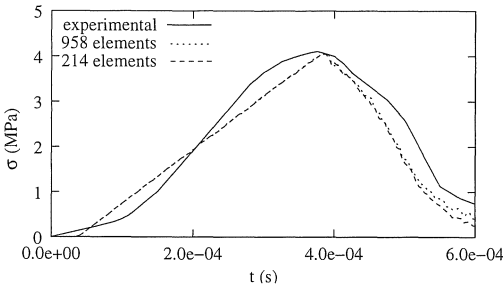


Figure 8: Calculated normal stress transmitted across at the top boundary of the specimen for the non-symmetric failure case and experimental results.

symmetric failure are shown in figure 8. Again, the two meshes yield almost identical results. Curiously, the responses for symmetric and non-symmetric failure are very similar.

The calculated crack paths for the coarse and fine meshes are shown in figure 9 for the case of non-symmetric failure. The analyses with the two meshes predict the same crack path and the crack path is completely independent of the mesh structure. To further compare the objectivity of the model with respect to spatial discretisation, the evolution of strain energy with time for the two meshes is shown in figure 10. The strain energy  $U$  is calculated by:

$$U = \int_{\Omega \setminus \Gamma_d} \boldsymbol{\varepsilon} : \boldsymbol{\sigma} \, d\Omega + \int_{\Gamma_d} \mathbf{t} \cdot \tilde{\mathbf{u}} \, d\Gamma \quad (22)$$

The results correspond to the symmetric failure mode. The results in figure 10 are indistinguishable for the two meshes, further illustrating the objectivity of the model with respect to spatial discretisation. Moreover, the results show not only the objectivity of the model with respect to spatial discretisation, but also that the model performs excellently with very coarse meshes.

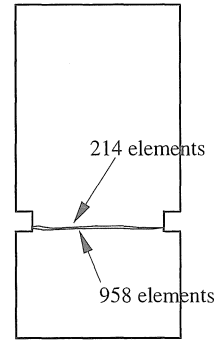


Figure 9: Calculated crack paths for the two meshes (non-symmetric failure).

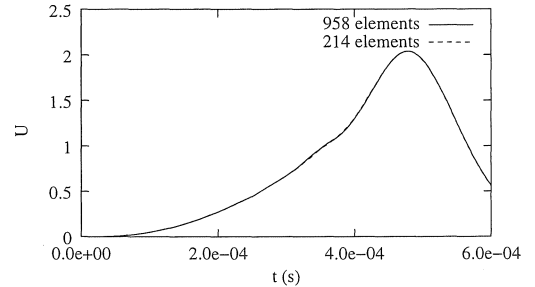


Figure 10: Evolution of the strain energy per unit thickness with time for symmetric failure of the double-notched specimen.

## 7 CONCLUSIONS

A recently developed numerical model for simulating cohesive zones has been extended for impact analyses. The model allows displacement discontinuities to pass arbitrarily through a finite element mesh. Displacement discontinuities are continuous across element boundaries and the order of interpolation of the jump is the same as the underlying finite element. The displacement jump is simulated by adding extra degrees of freedom to existing nodes near a discontinuity. The addition of a displacement discontinuity manifests itself in the stiffness matrix and the mass matrix of the discretised problem through the appearance of the Heaviside jump. This is in contrast to so-called ‘embedded discontinuity’ models, in which the effect of a displacement jump is added as in an incompatible strain mode, while the displacement field is continuous (therefore the consistent mass matrix is the same as for a continuum model). The mathematical soundness of the proposed model means that there are no limitations on the type of underlying base element.

Numerical examples have shown that the developed model is objective with respect to spatial discretisation, with the path of a cohesive crack completely in-

dependent of the mesh structure. The model is also extremely robust and effective under impact loading. Further, the numerical examples show that the model performs excellently with very coarse finite element meshes, making it ideal for large scale calculations.

#### ACKNOWLEDGEMENTS

This research is supported by the Technology Foundation STW, applied science division of NWO and the technology program of the Ministry of Economic Affairs and the Ministry of Public Works and Water Management, The Netherlands.

#### REFERENCES

- Babuška, I. and J. M. Melenk (1997). The Partition of Unity Method. *International Journal for Numerical Methods in Engineering* 40(4), 727–758.
- Barenblatt, G. I. (1962). The mathematical theory of equilibrium cracks in brittle fracture. *Advances in Applied Mechanics* 7, 55–129.
- Bažant, Z. P. and T. B. Belytschko (1985). Wave propagation in a strain-softening bar: Exact solution. *ASCE Journal of Engineering Mechanics* 111(3), 381–389.
- Duarte, C. A. and J. T. Oden (1996). H-p clouds – an h-p meshless method. *Numerical Methods for Partial Differential Equations* 12(6), 673–705.
- Dugdale, D. S. (1960). Yielding of steel sheets containing slits. *Journal of the Mechanics and Physics of Solids* 8, 100–108.
- Hillerborg, A., M. Modeer, and P. E. Petersson (1976). Analysis of crack formation and crack growth in concrete by means of fracture mechanics and finite elements. *Cement and Concrete Research* 6(6), 773–782.
- Schellekens, J. C. J. and R. De Borst (1993). On the numerical integration of interface elements. *International Journal for Numerical Methods in Engineering* 26(1), 43–66.
- Sluys, L. J. and R. De Borst (1996). Failure in plain and reinforced concrete – an analysis of crack width and crack spacing. *International Journal of Solids and Structures* 33(20–22), 3257–3276.
- Swenson, D. V. and A. R. Ingraffea (1988). Modeling mixed-mode dynamic crack propagation using finite elements: Theory and applications. *Computational Mechanics* 3(5), 381–397.
- Weerheijm, J. (1992). *Concrete under impact tensile loading and lateral compression*. Ph. D. thesis, Delft University of Technology.
- Wells, G. N. and L. J. Sluys (2001a). Discontinuous analysis of softening solids under impact loading. *International Journal for Numerical and Analytical Methods in Geomechanics* 25(6).
- Wells, G. N. and L. J. Sluys (2001b). A new method for modelling cohesive cracks using finite elements. *International Journal for Numerical Methods in Engineering* 50(12), 2667–2682.
- Wells, G. N. and L. J. Sluys (2001c). Three-dimensional embedded discontinuity model for brittle fracture. *International Journal of Solids and Structures* 38(5), 897–913.